ACS OMEGA

http://pubs.acs.org/journal/acsodf

Article

Theoretical Insights into the Geometrical Evolution, Photoelectron Spectra, and Vibrational Properties of YGe_n^- (n = 6−20) Anions: From Y-Linked to Y-Encapsulated Structures

Haibo Wang, Caixia Dong, and Jucai Yang*

Cite This: *ACS Omega* 2022, 7, 36330−36342

Read Online

ACCESS | Metrics & More | Article Recommendations | Supporting Information

ABSTRACT: The structural evolution behavior of germanium anionic clusters doped with the rare-earth metal yttrium, YGe_n^- (n = 6−20), has been investigated using a mPW2PLYP density functional scheme and an ABCluster structure searching technique. The results reveal that with increasing cluster size n, the structure evolution pattern is from the Y-linked framework (n = 10−14), where Y serves as a linker (the Y atom bridges two germanium subclusters), to the Y-encapsulated framework (n = 15−20), where the Y atom is located in the center of the Ge cage. The simulated PES spectra show satisfying agreement with the experimental PES spectra for n = 12−20, which reveals that the global minimum structures reported here are reliable. In particular, the anionic YGe_{16}^- nanocluster is found to be the most stable structure in the size range of n = 6−20 through analyzes of the relative stability, highest occupied molecular orbital (HOMO)−lowest unoccupied molecular orbital (LUMO) gap, spherical jellium model, and isochemical shielding surface. Moreover, spectral properties such as infrared and Raman spectra were reported. In addition, the UV−vis spectra of the YGe_{16}^- nanocluster are in good agreement with solar energy distribution, showing that such substances serve as multifunctional building blocks to be potentially used in optoelectronic devices or solar energy converters.

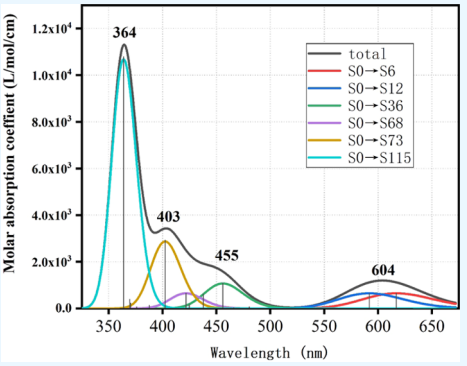

1. INTRODUCTION

Even if silicon contributed to the rise of microelectronics semiconductor industry, it was not the first material employed in such apparatuses. Germanium is well known for the construction of the first semiconductor triode in 1948.[1,2] Germanium as a microelectronics material is now of renewed interest owing to the fact that the charge mobility of germanium-based materials exceeds that of silicon-based materials by a factor of 3, offering an advantage for high-speed circuits and germanium-based detectors.[3] Furthermore, the germanium cluster plays a very important role in the field of infrared optics. It has the advantages of high infrared refractive index, wide infrared transmission band range, small absorption coefficient, and low dispersion rate.[4] To compare with the pure ones, introducing metal atoms, especially rare-earth atoms, into germanium materials is believed to bring improved properties.[5−7]

Rare earth is a general term for 15 lanthanide elements plus scandium and yttrium in the periodic table. They have properties such as high magnetic moments and extremely narrow optical transitions. For instance, rare-earth molecular crystals have excessively narrow optical transitions and long-lived quantum states, which enable them to be used in fields such as quantum communication and quantum processors, thereby opening up optical quantum systems.[8] Rare-earth metal (REM)-doped fiber amplifiers that amplify in the near- and mid-infrared spectral regions have been developed.[9,10] Introducing REM into Ge clusters not only enriches the properties of germanium-based materials but also causes synergistic effects to perfect the germanium-based material inherent properties, thereby getting new multifunctional nanostructured materials. Moreover, the stability of germanium clusters can be enhanced by introducing with REMs because pure germanium clusters holding only sp^3-hybridized bonding features are unstable.[11−13] As the building blocks of self-assembling semiconductors and other novel nanostructured materials, germanium-based clusters have been capaciously investigated according to small- and medium-sized Ge clusters doped with a transition metal atom in both theory and experiment.[14−34] In particular, "superatoms" as building blocks of cluster-assembled materials are the most basic artificial units. Compared with the limited stable elements that exist in nature, the types and number of superatoms are almost infinite. This is equivalent to expanding the scope of the periodic table of elements.[35,36] However, introducing REM into Ge clusters is

Received: June 25, 2022
Accepted: September 26, 2022
Published: October 6, 2022

https://doi.org/10.1021/acsomega.2c03983
ACS Omega 2022, 7, 36330−36342

not much investigated until now. It is expected to attract widespread interest because superatoms with the synergistic effect induced by doping with REM can result in multifunctional nanostructured materials with new properties such as magnetism, catalytic and photoelectric properties, etc.

From the experimental aspect, Atobe et al.[37] investigated the electronic properties of Ge clusters containing the REM atom $REMGe_n$ (REM = Sc, Y, Lu, n = 8−20) through anion photoelectron spectra (PES) and their reactivity to H_2O adsorption. They found that the threshold energy of electron detachment of $REMGe_n^-$ showed local maximum values at n = 10 and 16. From the theoretical aspect, Singh et al.[38] investigated $Th@Ge_n$ (n = 16, 18, and 20) clusters with an ab initio calculation, and their results highlighted the enhanced stability of $Th@Ge_{16}$ and $Th@Ge_{20}$. Specifically, they pointed out that $Th@Ge_{16}$ has a wide highest occupied molecular orbital (HOMO)/lowest unoccupied molecular orbital (LUMO) gap of 1.72 eV that makes it fascinating for optoelectronic applications. Recently, Yang et al.[6,30,39] studied the structural evolution and electronic properties of introducing a Lu atom into Ge_n (n = 5−17) compounds in neutral, anionic, and cationic states and found that the ultraviolet−visible (UV−vis) spectra of $LuGe_{16}^-$ and $LuGe_{17}^+$ clusters match with solar energy distribution, which make them the most suitable building blocks for potentially usage in solar energy converters or ultrahigh-sensitive near-infrared photodetectors. More recently, the spatial structure and electron energy spectra of Gd-doped anionic Ge_n^- clusters have been reported.[40] Here, a global search algorithm and a double-hybrid density functional were applied for geometric optimization for introducing Y into Ge anionic clusters (YGe_n^- (n = 6−20)) with the purpose of combing their global minimum (GM) structure features and evolutions, simulating their PES, infrared, Raman, and specific-sized ultraviolet−visible (UV−vis) spectra and comparing simulated PES spectra with previous experimental ones.[37] The simulated PES spectra for GM structures match with those measured in the experiment, indicating that the current ground-state structures exist in the experiment. In addition, the HOMO−LUMO gaps were evaluated. The findings of this study could enrich the understanding of rare-earth metal-doped Ge clusters, which are extremely important for synthesizing novel multifunctional materials.

2. COMPUTATIONAL DETAILS

The starting isomer search for YGe_n^- (n = 6−20) nanoclusters stems from two ways: (i) First, utilizing an ABCluster unprejudiced search algorithm[41−43] in association with the Gaussian 09 program package,[44] more than 400 configurations for each YGe_n^- (n = 6−20) nanocluster randomly generated by the ABCluster were optimized with the PBE0[45] functional. The basis set used is BS-1 (BS-1: cc-pVDZ-PP basis set[46] for Ge atoms and LanL2DZ basis set[47] for Y atoms). Second, the acquired low-lying structures were reoptimized through the PBE0 functional combined with the BS-2 basis set (BS-2: relativistic effective core pseudopotential cc-pVTZ-PP basis set[46] for Ge atoms and quasi-relativistic ab initio effective core potential ECP28MWB basis set[48,49] for Y atoms). At the same level, frequency analyzes were executed to guarantee that the isomers were true local minimal structures. (ii) Geometries presented in the literature[39,50] were calculated using the PBE0/BS-II scheme if they did not emerge in the outcomes of the ABCluster. Behind completing the initial geometry optimization through the PBE0 scheme, for a second time, we picked the low-lying contenders and reoptimized them using a double hybrid mPW2PLYP functional[51] and BS-2 basis set. At the mPW2PLYP/BS-2 level, frequency analyzes were not executed owing to the limited computed capacity and saving calculation time. At length, single-point energy calculations were executed through the mPW2PLYP/BS-3//mPW2PLYP/BS-2 scheme to further refine the energies (BS-3: aug-cc-pVTZ basis set[52] for Ge atoms and ECP28MWB basis set[48,49] for Y atoms). The PES spectra of YGe_n^- (n = 6−20) species were simulated via the Multiwfn software package[53] based on the outer-valence Green function (OVGF) scheme[54] in conjunction with the ECP28MWB basis set[48,49] for Y atoms and aug-cc-pVDZ basis set[52] for Ge atoms. Simulations of vibrational spectra with infrared (IR) and Raman activity were executed at the PBE0/BS-2//mPW2PLYP/BS-2 level for the GM structures whose theoretical PES spectra match those measured in the experiment.

Only singlet spin multiplicities for YGe_n^- (n = 6−20) clusters were taken into account in light of the following case. The ground state of Ge atoms is triplet (^3P). The spin multiplicity of the most stable structure of the YGe^- anion is triplet ($^3\Pi$), which is more stable than that of singlet ($^1\sum$) by 0.19 eV in energy. The ground state of Ge_2 molecules is also triplet ($^3\sum_g$). The spin multiplicity of the GM structure of the YGe_2^- compound (isosceles triangle) is also triplet ($^3B_2$), which is more stable in energy than that of the $^1A_1$ electronic state by 0.53 eV. Singlet and triplet spin multiplicities compete with each other for the ground-state structure of the Ge_3 cluster. The $^1A_1$ electronic state (isosceles triangle) is more stable in energy than that of $^3A_1'$ (regular triangle) by 0.06 eV at the CCSD(T)/aug-cc-pVTZ//B3LYP/6−311 + G(d) level.[11] The spin multiplicity of the GM configuration of the YGe_3^- cluster (rhombus) is singlet ($^1A_1$), which is more stable in energy than that of triplet ($^3A_2$) by 0.45 eV. Starting from n = 4, the spin multiplicity of the GM structure Ge_n with $n \leq 20$ is singlet.[11,12] The spin multiplicity of the GM geometry of YGe_4^- (trigonal bipyramid) and YGe_5^- (tetragonal bipyramid) clusters is singlet ($^1A_1$). This indicates that only introducing Y^- into a Ge_n cluster of triplet spin multiplicity can produce a YGe_n^- cluster in the triplet ground state, that is, the ground states of YGe_n^- (n = 6−20) clusters are singlet. All the same, we evaluated the energies of the triplet for YGe_n^- (n = 6−20) clusters and list them in Table S1 in the Supporting Information. We can see from it that the energies of the triplet are larger than those of the singlet. Consequently, only singlet spin multiplicities for YGe_n^- (n = 6−20) clusters were reported.

For the sake of justifying the reliability of our calculations, checkout calculations had formerly been completed via the ROCCSD(T) method for $ScSi_n^{0/-}$ (n = 4−9) compounds and compared them with several different DFT functions.[55] The outcomes confirmed that only the most stable structures and vertical detachment energy (VDE) of $ScSi_n^{0/-}$ compounds calculated via the mPW2PLYP approach agree with those of the ROCCSD(T) approach. In addition, the bond distances of Ge_2, AgGe, and AuGe species evaluated by the mPW2PLYP scheme are 2.38,[56] 2.45,[56] and 2.34 Å, respectively.[57] They are in agreement with experimental bond distances of 2.368,[58] 2.54,[59] and 2.38 Å.[60] The frequencies calculated at the PBE0 functional are 290.7 cm^{-1} for Ge_2 in the $^3\sum_g$ state, 317 cm^{-1} for Ge_2^- in the $^2\Pi_u$ state, and 333 cm^{-1} for Ge_2^- in the $^2\sum_g$ state. They are in agreement with experimental data of 286 ±

https://doi.org/10.1021/acsomega.2c03983
ACS Omega 2022, 7, 36330−36342

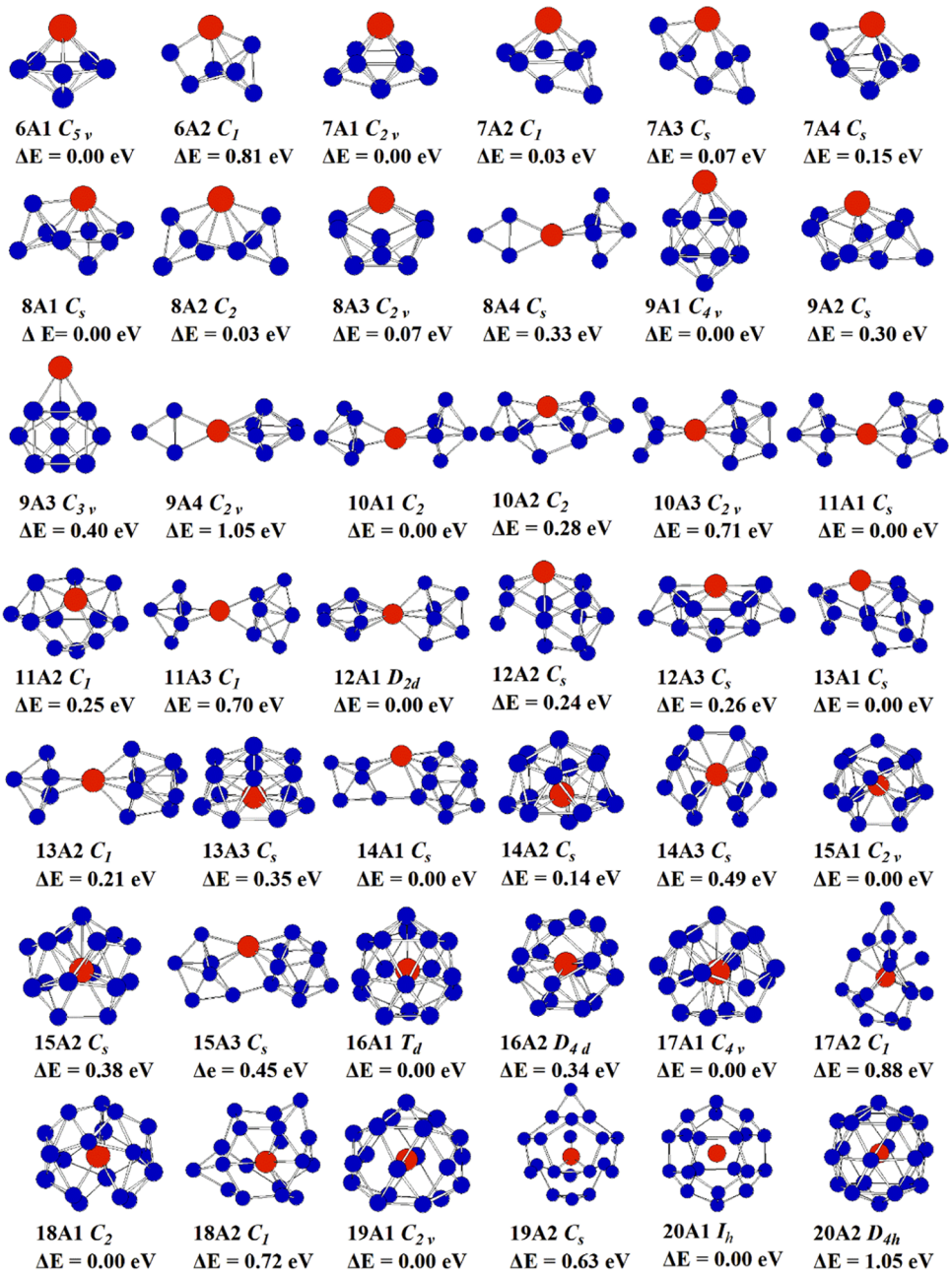

Figure 1. Stable configurations of the anionic YGe_n^- (n = 6−20) clusters. The red and blue circles (color online) symbolize yttrium and germanium atoms, respectively.

5, 309 ± 5, and 326 ± 10 cm^{-1}.[61] Consequently, the present methodology can legitimately describe the properties of YGe_n^- nanoclusters.

3. RESULTS AND DISCUSSION

3.1. Structural Evolution and Characteristics of YGe_n^- Nanoclusters. All chosen frameworks including GM and low-lying frameworks of doped Ge anionic clusters with Y atoms are shown in Figure 1. The clusters are appointed as nAm, with n standing for the number of Ge atoms, A standing for anions, and m standing for the number of clusters, in light of their energy ascending. For n = 6, the pentagonal bipyramid (**6A1**) in the $^1A_1$ ground state is predicted to be the GM structure analogous to the YSi_6^- cluster.[50] For n = 7, similar to the YSi_7^- cluster,[50] two isomers (**7A1** and **7A2**) compete with each other for the ground state. The **7A1** bi-face-capped tetragonal bipyramid in the $^1A_1$ electronic state is only slightly more stable in energy than the **7A2** capped pentagonal bipyramid by 0.03 eV. This indicates that the potential energy surfaces of the YGe_7^- cluster are very flat, that many isomeric arrangements are possible, and that accurate predictions of equilibrium geometries require the combination of experimental research and theoretical simulation because the problem of shallow potential energy surfaces cannot be solved by advanced quantum mechanical calculation methods. Therefore, we simulated PES, IR, and Raman spectra of **7A1** and **7A2** clusters (see below) to lay the ground for experimental studies. For n = 8, similar to n = 7, two isomers (**8A1** and **8A2**) compete with each other for the most stable structure. The **8A1** geometry can be regarded as attaching Ge_2 to the most

https://doi.org/10.1021/acsomega.2c03983
ACS Omega 2022, 7, 36330−36342

stable structure of the YGe_6 cluster. The **8A2** isomer, similar to the ground state structure of the YSi_8^- cluster,[50] is a linked structure, in which the Y atom links two Ge_4 tetrahedrons. In the ^1A electronic state, it is only slight less stable in energy than **8A1** in the $^1A'$ electronic state by 0.03 eV, that is, the potential energy surface of the YGe_8^- cluster is also very flat. For n = 9, the GM structure is predicted to be a bi-face-capped (one of them is a metal atom) tetragonal antiprism (**9A1**) of the $^1A_1$ ground state analogous to the ground state structure of the YSi_9^- cluster.[50]

For n = 10, similar to the YSi_{10}^- cluster,[62] the GM configuration is the linked structure (**10A1**) of the ^1A ground state in which the Y atom links two orthogonal Ge_5 trigonal bipyramids. The **10A2** isomer, similar to 10c geometry in ref 40, is also a linked structure. **10A3** is a linked configuration, in which the Y atom connects a Ge_4 subcluster and a capped trigonal bipyramid. Energetically, they are less stable in energy than that of **10A1** by 0.28 and 0.71 eV, respectively. For n = 11, 12, and 14, similar to YSi_{11}^-, YSi_{12}^-, and YSi_{14}^- clusters reported by Liu et al.,[62] their GM configurations are linked structures. The Y atom in the YGe_{11}^- cluster of the $^1A'$ ground state connects a Ge_5 trigonal bipyramid and a Ge_6 capped trigonal bipyramid, that in the YGe_{12}^- cluster of the $^1A_1$ ground state connects two orthogonal Ge_6 subclusters, and that in the YGe_{14}^- cluster of the $^1A'$ ground state connects a Ge_5 subcluster and a Ge_9 tricapped trigonal prism (TTP). For n = 13, the GM geometry, similar to the YSi_{13}^- cluster,[50] is a linked structure of the $^1A'$ ground state, in which Y joins a Ge_4 distorted tetrahedron and a Ge_9 TTP.

For n = 15, the GM configuration is predicted to be a Y-doped Ge cage-like motif (**15A1**) consisting of 2 pentagonal faces and 10 quadrangles (TPTQ). It can be viewed as being derived from the Frank−Kasper (FK) cage of Ge_{16} (see **16A1**) through removing a Ge atom, denoted as the FK-cage. It is C_{2v}-symmetry in the $^1A_1$ ground state. The **15A2** cage can be viewed as being derived from the fullerene cage of Ge_{16} (see **16A2**) via eliminating a Ge atom, denoted as the f-cage. It is less stable in energy than the FK-cage by 0.38 eV. The C_s-symmetry **15A3** of the $^1A'$ electronic state, similar to the ground-state structure of the YSi_{15}^- cluster,[50,62] is a linked configuration in which the Y atom joins a Ge_6 capped trigonal bipyramid and a Ge_9 TTP. Energetically, it is less stable than the FK-cage by 0.45 eV. For n = 16, the GM configuration is evaluated to be Y-encapsulated into the Ge_{16} FK-cage (**16A1**) with T_d symmetry and $^1A_1$ ground state. The D_{4d} symmetry **16A2**, similar to the most stable structure of the YSi_{16}^- cluster,[50,62] is a Y-doped Ge_{16} f-cage. However, vibrational analyzes yield four imaginary frequencies. It undergoes Jahn−Teller distortion to give a C_1 symmetry isomer, which is actually the **16A1** FK-cage. For n = 17, the GM motif is calculated to be a Y-encapsulated polyhedron of five-capped four pentagonal faces and two quadrangles (**17A1**) with C_{4v} symmetry in the $^1A_1$ ground state. The structure optimization using the most stable geometry of the YSi_{17}^- cluster[50] as the initial geometry of the YGe_{17}^- cluster shows that there is an imaginary frequency. Following the imaginary frequency mode, it collapses to the **17A2** isomer. It is 0.88 eV above the **17A1** structure. For n = 18, the GM geometry is a Y-encapsulated endohedral configuration (**18A1**) with C_2 symmetry in the ^1A ground state. Using the GM of the YSi_{18}^- cluster[62] as the initial structure optimization of the YGe_{18}^- cluster, vibrational analysis yields more than one imaginary frequencies. It undergoes Jahn−Teller distortion to give the **18A2** isomer. It is less stable in energy than 18A1 by 0.72 eV. For n = 19, its GM structure (**19A1**) is a Y-encapsulated endohedral motif with C_{2v} symmetry in the $^1A_1$ ground state. Using the most stable structure of the YSi_{19}^- cluster[62] as the initial structure optimization of the YGe_{19}^- cluster, the C_s-symmetry **19A2** isomer of $^1A'$ can be obtained. It is 0.63 eV above the **19A1** structure. For n = 20, a pentagonal dodecahedron with I_h symmetry and ^1A_g ground state is predicted to be the GM structure (**20A1**), analogous to the YSi_{20}^- cluster.[62] It is more stable in energy than the D_{4h} symmetry **19A2** of the $^1A_{1g}$ electronic state by 1.05 eV.

From the results presented above, it is evident that the GM structural evolution favors Y-linked structures, in which the metal atom bridges two Ge subgroups when n = 10−14 and the Y-encapsulated Ge cage-like framework is favored when n = 15−20. Compared with Y-doped anionic silicon clusters, the common feature is that the structural evolution is from metal atom-linked to metal atom-encapsulated structures. There are two differences. One is that the threshold sizes for the formation of the cage are different. It is n = 15 for germanium clusters, and it is n = 16 for silicon clusters. The radius of germanium is larger than that of silicon, so the threshold size for the formation of the Ge cage is smaller than that of the Si cage. The other is that Ge cages prefer the FK-structure feature and Si cages prefer the f-structure feature.

The stability of YGe_n^- clusters can be explained using the spin-polarized electronic structures, similar to Y-doped Si_n^- clusters.[50] Ge subgroups in the Y-linked forms are a tetrahedron of Ge_4, trigonal bipyramid of Ge_5, tetragonal bipyramid of Ge_6, and TTP of Ge_9. Therefore, the electronic configurations with spin polarization of Ge_4, Ge_5, Ge_6, and Ge_9 are predicted[39] (also, see Figure S1 in the supporting information). One can see from the figure that the up-spin spectrum of Ge_5 has a big energy gap between the HOMO and the LUMO and that there are two unoccupied MOs in the down-spin spectrum within the scope of the HOMO and the LUMO. It indicates that subgroup Ge_5 demands two electrons to be stabilized. Thanks to the fact that the Y^- anion possesses four valence electrons, it can connect a pair of Ge_5 subgroups in such a way that each Ge_5 possesses a pair of holes in the HOMO. The Y^- negatively charged ion in the **10A1** linked form offered (or shared) four electrons (two electrons to each Ge_5), bringing about the stability of the **10A1** motif. The spin-polarized electron structure of Ge_6 is consistent with that of Ge_5. Therefore, two electrons of anionic Y^- in **11A1** and **12A1** participated with Ge_5 and Ge_6, respectively, bringing the stability of **11A1** and **12A1** linked structures. With regard to tetrahedral Ge_4 and TTP Ge_9, their spin-polarized electron structures are different from those of Ge_5 and Ge_6. There are four unoccupied states in the down-spin spectrum in the range of the up-spin spectrum of Ge_4 and Ge_9. It indicates that subgroups Ge_4 and Ge_9 demand four electrons to be stabilized. In the **13A1** linked form, the Y^- negatively charged ion offered (or shared) four electrons (two electrons to Ge_4 and Ge_9). Meanwhile, Ge_4 and Ge_9 are joined through two Ge atoms. Thus, two electrons on each participating Ge atom contribute to Ge_4 and Ge_9, bringing the stability of **13A1**. In the **14A1** linked form, Ge_5 demands two electrons to be stabilized, but Ge_9 demands four electrons to be stabilized. Therefore, the GM structure begins to favor the Y-encapsulated framework.

3.2. PES of YGe_n^- Anionic Clusters. At this stage, it is compelling to verify the validity of the determined GM configurations. In addition, PES spectra are extremely

https://doi.org/10.1021/acsomega.2c03983
ACS Omega 2022, 7, 36330−36342

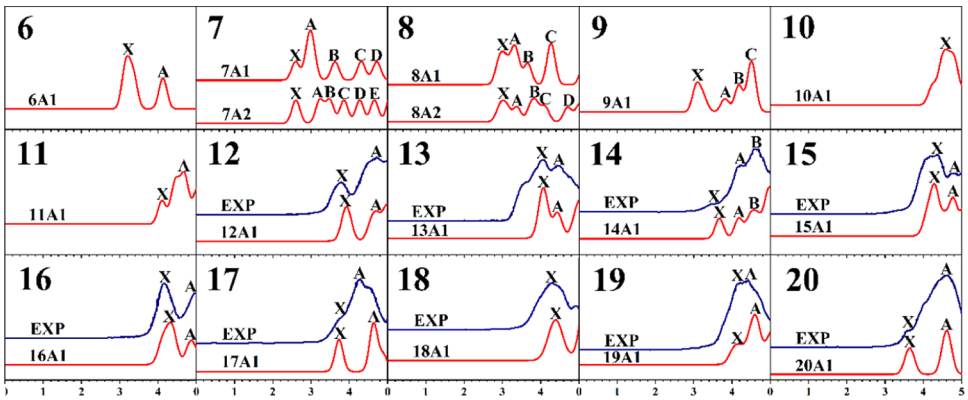

Figure 2. Simulated PES spectra of the lowest-lying energy configurations of YGe_n^- (n = 6−20) clusters. Experimental PES reprinted with permission from ref 37.

important data to extract electronic binding energies from the ground-state structures of atomic and molecular clusters, which can give more valuable information about the underlying electronic structures. In particular, there is no experimental approach for directly determining the GM configuration of atomic and molecular clusters up to now. To verify the GM configurations of Y-doped Ge anionic clusters, the PES spectra of YGe_n^- (n = 8−20) clusters are simulated using OVGF[54] and compared with the available experimental results. In the PES simulation, to fit all peaks in the region of less than 5.00 eV, Gaussian full width at half maximum (FWHM) values of 0.25 eV for n = 8−14 and 0.30 eV for n = 15−20 are utilized. Two criteria in comparing the simulated and experimental PES spectra are used: (a) first VDE and (b) the number of distinct peaks and their relative locations in the PES spectra. The theoretical PES spectra together with the experimental PES spectra are displayed in Figure 2. The calculated and experimental first VDEs are tabulated in Table 1. From Figure 2 and Table 1, we can see satisfactory overall agreement between simulated and available experimental data, suggesting the validity of our theoretical approach and reliability of our results.

Table 1. Theoretical and Experimental Vertical Detachment Energy (VDE, in eV) for YGe_n^- Clusters

	VDE (eV)			VDE (eV)	
species	theor.	exp.[a]	species	theor.	exp.[a]
6	3.21		13	4.00	4.03 ± 0.10
7	2.71		14	3.65	3.56 ± 0.15
8 (**A1**)	3.00		15	4.28	4.35 ± 0.15
8 (**A2**)	3.02		16	4.32	4.18 ± 0.10
9	3.10		17	3.76	3.73 ± 0.15
10	4.59		18	4.42	4.32 ± 0.10
11	4.11		19	4.16	4.17 ± 0.15
12	3.93	3.80 ± 0.10	20	3.64	3.64 ± 0.10

[a]Experimental VDE taken from ref 37.

For n = 20, its simulated PES spectra show two distinct peaks residing at 3.64 and 4.61 eV, which are in excellent agreement with experimental data of 3.64 and 4.60 eV, respectively.[37] In the simulated PES of n = 19, two major peaks located at 4.16 and 4.60 eV are also observed. They match with experimental values of 4.17 and 4.43 eV.[37] In the case of n = 18, only one peak at 4.42 eV is obtained in the range of less than 5.00 eV. It reproduces an experimental value of 4.32 eV.[37] In the case of n = 17, there are two different peaks situated at 3.73 and 4.64 eV. Only the first peak is in excellent agreement with the experimental counterpart of 3.76 eV.[37] The second peak does not match with the experimental value of 4.29 eV.[37] For n = 12, 13, 15, and 16, their simulated PES spectra also have two distinct peaks located at 3.93 and 4.70, 4.00 and 4.31, 4.28 and 4.77, and 4.32 and 4.87 eV, which match with the experimental data of 3.80 and 4.71, 4.03 and 4.43, 4.35 and 4.77, and 4.18 and 4.95 eV,[37] respectively. In the case of n = 14, three different peaks were situated at 3.65, 4.17, and 4.53 eV. They successfully reproduced experimental features of 3.56, 4.21, and 4.57 eV, respectively.[37] Quantitative analyzes from Table 1 revealed that the average absolute deviation of the calculated first VDEs from the experiment is only 0.07 eV. The largest deviation is that of the YGe_{16}^- cluster, which is off by 0.14 eV. The satisfactory agreement between the calculated and experimental VDE and PES spectra reveals that the current GM configurations are present in the experiment.

For n = 11 and 6, two distinct peaks (X, A) are located at 4.11 and 4.67 and 3.21 and 4.13 eV, respectively. In the simulated PES n = 10, only one peak at 4.59 eV is observed in the range of less than 5.00 eV. In the case of n = 9, there are four peaks (X, A−C) residing at 3.10, 3.82, 4.18, and 4.51 eV. For n = 8, two energetically degenerate configurations are simulated. In the simulated PES of **8A1**, there are four peaks (X, A−C) situated at 3.00, 3.31, 3.65, and 4.27 eV, but there are five peaks (X, A−D) located at 3.02, 3.37, 3.82, 4.06, and 4.71 eV in the case of the **8A2** isomer. It is difficult to distinguish the two isomers with the position of the peaks because the positions of the first four peaks are almost identical. It is possible for them to coexist in the experiment. For n = 7, similar to n = 8, two structures are simulated. There are five peaks (X, A−D) in the simulated PES of **7A1**. They are located at 2.60, 2.98, 3.63, 4.31, and 4.71 eV, respectively. In the case of **7A2**, there are six peaks (X, A−E) situated at 2.60, 3.24, 3.47, 3.86, 4.27, and 4.65 eV, respectively. The first VDEs of **7A1** and **7A2** are very close and the smallest among these investigated clusters. For n = 6−11 clusters, there are no experimental counterparts for comparison. We hope that our theoretical simulations will provide useful information for further experimental research.

3.3. Relative and Chemical Stability. The instinctive stability of clusters considered can be inspected via the average binding energy (ABE). It is defined as follows

https://doi.org/10.1021/acsomega.2c03983
ACS Omega 2022, 7, 36330−36342

$$\mathrm{ABE}(YGe_n^-) \rightarrow [(n-1)E(\mathrm{Ge}) + E(\mathrm{Ge}^-) + E(\mathrm{Y}) - E(YGe_n^-)]/(n+1) \quad (1)$$

where $E(\mathrm{Ge})$, $E(\mathrm{Ge}^-)$, $E(\mathrm{Y})$, and $E(YGe_n^-)$ are the total energy corresponding to the respective atoms and/or anions. ABE against the corresponding cluster size is depicted in Figure 3a. It indicates the energy gain of adding a neutral Ge atom to an existing cluster. A larger ABE value of a cluster indicates higher stability. Therefore, the clusters of n = 9, 12, and 16 are more stable than those of n = 7, 10, 13, and 19 due to the fact that the ABEs are local maxima for n = 9, 12, and 16 and local minima for n = 7, 10, 13, and 19. It is noted that YGe_9^- and YGe_{12}^- clusters have only good relative stability, not the best thermodynamic stability. However, the YGe_{16}^- nanocluster not only has good relative stability but also possesses the best thermodynamic stability owing to the fact that its ABE is the largest.

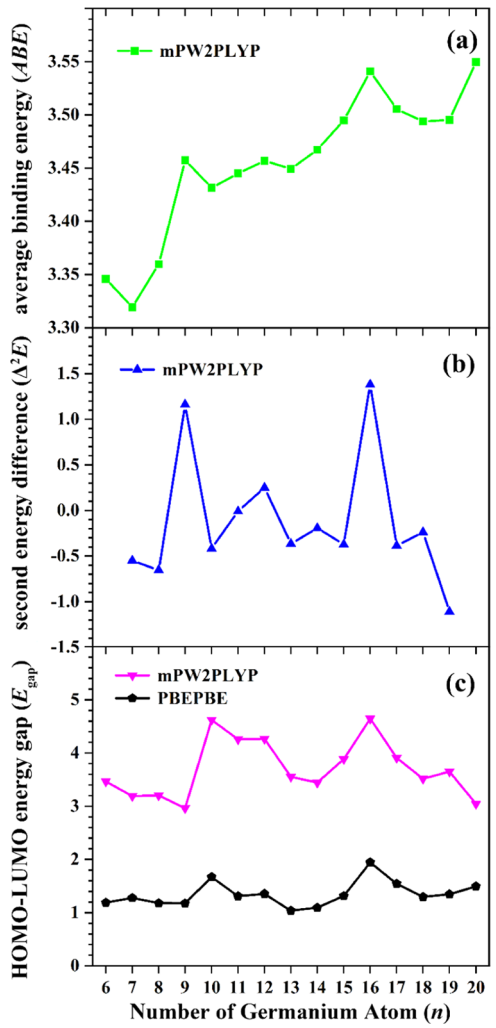

Figure 3. Size dependence of (a) average binding energy (ABE); (b) second energy difference (Δ^2E); and (c) HOMO−LUMO energy gap (E_{gap}).

Apart from the ABE, it is also explanatory to take into account the second energy difference (Δ^2E) to compare the stability of various clusters. It is defined as

$$\Delta^2E(YGe_n^-) \rightarrow E(YGe_{n+1}^-) + E(YGe_{n-1}^-) - 2E(YGe_n^-) \quad (2)$$

The Δ^2E values are shown in Figure 3b. The smaller the Δ^2E, the weaker the relative stability. From Figure 3b, we can see that Δ^2E is a susceptible measure, and it reproduced clearly the results of ABE shown in Figure 3a.

Along with the discussion mentioned above, it is also significant to know the chemical stability of YGe_n^- clusters. As is well known, the chemical stability can be mirrored by an important physical parameter, HOMO−LUMO energy gap (E_{gap}). In view of this, the E_{gap} values have been calculated at the PBE pure density functional theory (DFT) level. The reason for choosing the PBE scheme is that (i) the E_{gap} evaluated through pure DFT is closer to the real optical gap than that predicted via hybrid DFT[63] and (ii) the E_{gap} of Ge_n^- ($3 \le n \le 20$) obtained using the PBE scheme matches well that in the experiment.[13] The E_{gap} as a function of cluster size is plotted in Figure 3c. From the figure, we can observe that (i) the E_{gap} curve assessed via the mPW2PLYP and PBE is in gross parallel and the mPW2PLYP E_{gap} is on average larger than that of PBE by 2.33 eV and (ii) the E_{gap} values of YGe_n^- (n = 6−20) compounds range from 0.77 eV (YGe_7^-) to 1.94 eV (YGe_{16}^-). The first two largest are YGe_{16}^- (1.94 eV) and YGe_{10}^- (1.67 eV). A large E_{gap} value is a signature of the chemical stability, as the cluster wants to neither receive nor donate electrons. Hence, the YGe_{16}^- nanocluster possesses good chemical stability.

For the sake of understanding the charge transfer between the Y atom and the host of the Ge cluster, NPA (natural population analysis) of the YGe_n^- (n = 6−20) nanoclusters was executed through the mPW2PLYP/BS-3//mPW2PLYP/BS-2 scheme. The outcomes of the charge on the Y atom and the NPA valence configurations are scheduled in Table S2 in the Supporting Information. We can observe from it that the valence configuration of the Y atom in small-sized YGe_n^- (n = 6−9) compounds is $5s^{0.42-0.69}4d^{1.47-1.88}5p^{0.33-0.49}$. The charge of the Y atom in small-sized YGe_n^- (n = 6−9) ranges from +0.13 to +0.44 a.u., indicating that Y serves as an electron donor. In Y-linked frameworks (n = 10−14), the valence configuration of the Y atom is $5s^{0.36-0.43}4d^{1.60-2.09}5p^{0.63-0.86}$. The charge of the Y atom in n = 10−14 is +0.30, +0.01, −0.36, −0.03, and −0.01 a.u., implying that Y in the YGe_{10}^- cluster serves as an electron donor but an electron acceptor in the YGe_{12}^- cluster. In linked frameworks (n = 10−14), the valence configuration of the Y atom is $5s^{0.36-0.43}4d^{1.60-2.09}5p^{0.63-0.86}$. The charge of the Y atom in n = 10−14 is +0.30, +0.01, −0.36, −0.03, and −0.01 a.u., implying that Y in the YGe_{10}^- cluster serves as an electron donor but an electron acceptor in the YGe_{12}^- cluster. In Y Y-encapsulated frameworks, the valence configuration of the Y atom is $5s^{0.35-0.41}4d^{3.59-5.36}5p^{1.42-2.03}$.The charge always transfers from the Ge nanocluster to the Y atom, and the transferred charge ranges from 2.48e (in YGe_{20}^-) to 4.93e (in YGe_{16}^-), indicating that the Y atom serves as an electron acceptor.

Taking into account the discussions mentioned above, the enhanced stability and large E_{gap} observed on the YGe_{16}^- nanocluster can be rationalized within the cooperative effect of the electronic configuration and geometric framework. On the ground of the spherical jellium model, the 68 magic number valence electrons for the YGe_{16}^- nanocluster occupy the superatomic orbitals of $(1S)^2(1P)^6(1D)^{10}(1F)^{14}(2S)^2(1G)^{14}(2P)^6(1G)^4(2D)^{10}$ as shown in Figure 4, in which the 1S shell is characterized by σ bonds stemming from the Ge 4s and Y 5s and the 2S shell is characterized by π bonds between the p-orbitals of Ge atoms

https://doi.org/10.1021/acsomega.2c03983
ACS Omega 2022, 7, 36330−36342

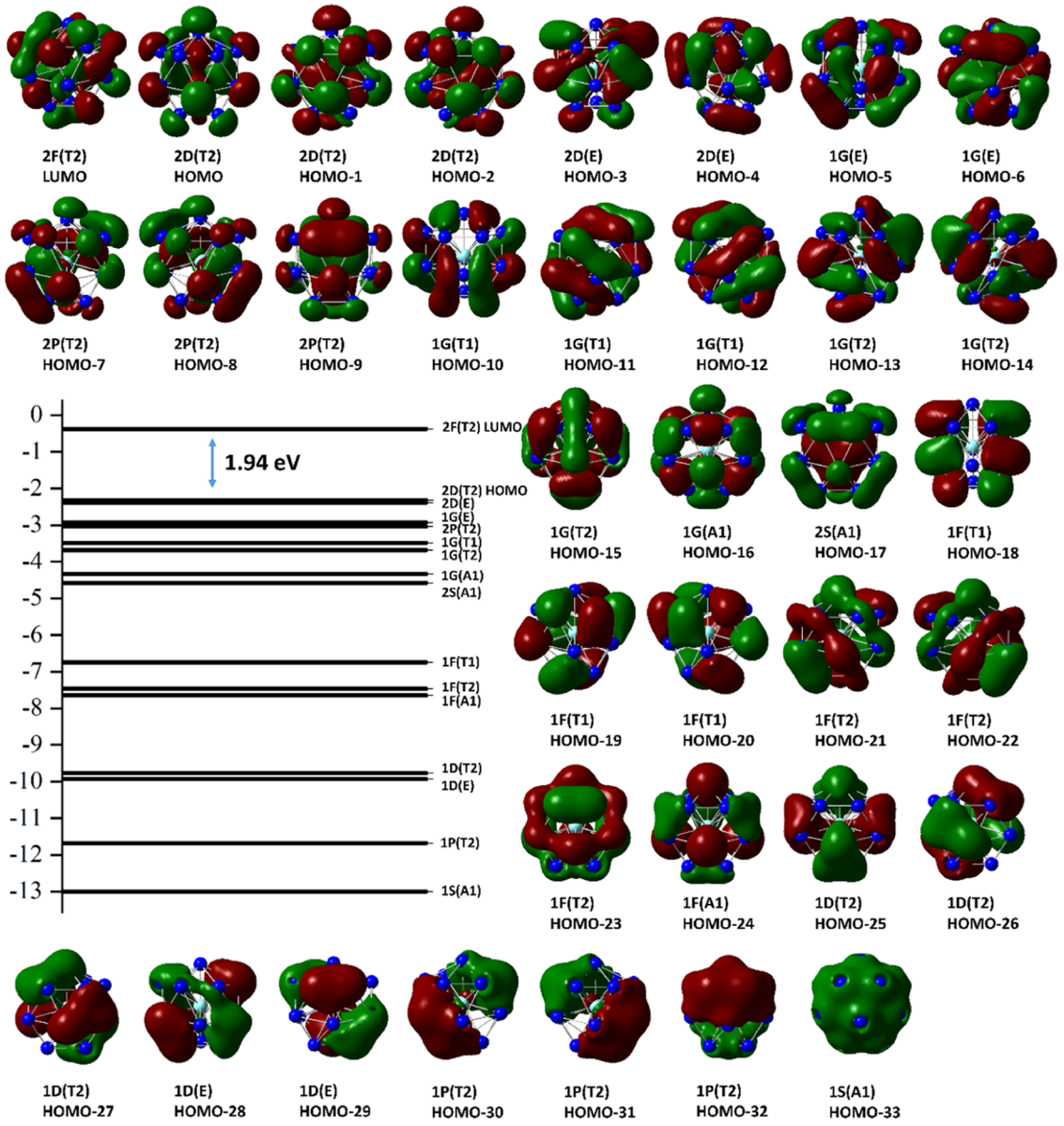

Figure 4. Molecular orbital charts of the HOMOs and LUMOs of the YGe_{16}^- nanocluster.

and the d-orbitals of the Y atom. The 1P shell is threefold degenerate and features π bonds mainly derived from the Ge 4p and Y 4d. The 2P shell is also threefold degenerate. It features π+σ bonds primarily coming from Ge 4s4p and Y 4d. The 1D and 2D shells are split into two sets of orbitals; one is threefold degenerate and another is double degenerate. They are $\pi + \sigma$ bonds formed greatly by 4s and 4p of the Ge atoms. The 1F and 1G shells are also $\pi + \sigma$ bonds formed mostly by 4s and 4p of the Ge atoms. Apart from the electronic configuration, the FK cage configuration of Ge_{16}^{4-} possesses aromaticity,[64] which may be the source of the stability of YGe_{16}^- nanocluster.

To further appreciate the stability of the YGe_{16}^- nanocluster, the isochemical shielding surface (ICSS)[65] in light of the real-space function is evaluated via a gauge-independent atomic orbital (GIAO) scheme. The outcomes are analyzed using Multiwfn software[53] and shown in Figure 5. In Figure 5A, the red section is the shielding region with an isovalue of 0.06 ppm, and the blue section is the deshielding region with an isovalue of 0.06 ppm. We can see from it that the red and blue sections have symmetry because the YGe_{16}^- nanocluster has a high symmetry of T_d. The shielding regions are displayed by three protruding red sections, and the red sections fill the whole real space of the YGe_{16}^- cage, indicating that the chemical shielding opposes the external magnetic field and that the interior of the cage has strong aromaticity. The ICSS variations of the YGe_{16}^- nanocluster with the distance from the center are shown in Figure 5B. It shows that the shielding values of the interior of the cage are larger than those of the outside of the cage. The maximal shielding value of 79.0 ppm resides at a distance of 1.1 Å from the core. In a word, examination of ICSS can be employed for aromaticity of the YGe_{16}^- nanocluster, which is one of the principal reasons of its enhanced stability.

In addition to the ICSS, it is also illustrative to consider the adNAP analysis[66] to further appreciate the stability of the YGe_{16}^- nanocluster. The objects of chemical bonding in the adNAP scheme are n-center 2-electron bonds, where n ranges

https://doi.org/10.1021/acsomega.2c03983
ACS Omega 2022, 7, 36330−36342

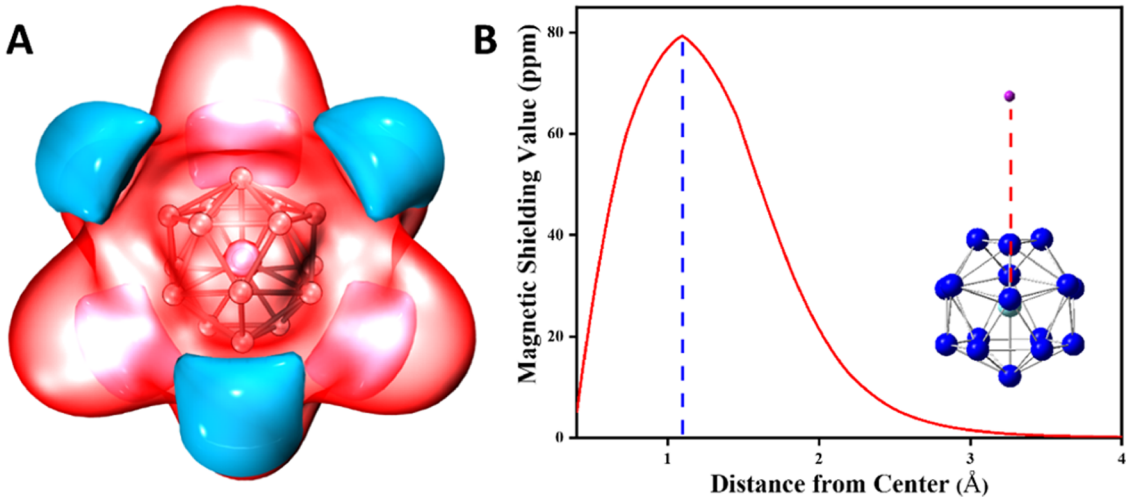

Figure 5. ICSS of the YGe16- nanocluster. (A) Isosurface of ICSS with an isovalue of 0.06 ppm (red section) and −0.06 ppm (blue section); (B) ICSS curve map of the magnetic shielding value with distance from the center.

from 1 (lone pair) to the maximum number of atoms in the cluster. The chemical bonding of 68 valence electrons for the T_d-symmetry YGe_{16}^- cluster is classified into three types, as shown in Figure 6: lone pair, 2c−2e, and 4c−2e. The Ge atom

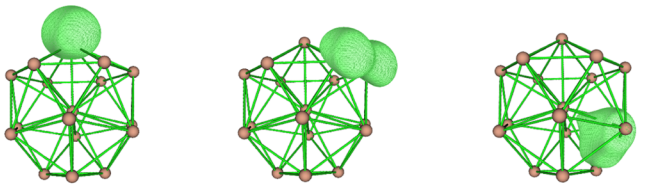

Figure 6. adNDP analysis of the YGe_{16}^- nanocluster. ON represents the occupation number.

residing on each of the four triad axes possesses a lone pair. Except for these four Ge atoms, the remaining 12 Ge atoms are characterized by 18 2c−2e localized Ge−Ge σ bonds with 1.89−1.91 electrons in each bond. The last type contains 12 delocalized 4c−2e σ bonds, which combines the central Y atom with the outer FK Ge_{16} shell and stabilizes the fully encapsulated YGe_{16}^- nanocluster.

3.4. Infrared and Raman Spectra. Apart from PES, infrared (IR) and Raman spectra are also one of the effective technologies to indirectly determine the GM structures. The IR and Raman spectra of YGe_n^- (n = 6−20) clusters were computed using the PBE0 functional to better understand their vibrational features. They are shown in Figure 7. The YGe_6^- compound is part of the C_{5v} point group symmetry. One and two dominant peaks in IR and Raman spectra are observed, respectively. The most intense IR frequency located at 103 cm^{-1} stems from the lowest doubly degenerate bending vibration mode of YGe_6. Two sharp peaks situated at 172 cm^{-1} and the largest wavenumber of 227 cm^{-1} being Raman active result from the axial stretching and breathing modes of YGe_6, respectively. For n = 7, two isomers are calculated. The **7A1** structure falls into the C_{2v} point group symmetry category. In IR spectra, the most intense peak at 222 cm^{-1} stems from the bending vibration of YGe_7 (Ge atom on the symmetry axis does not move). The second strongest peak at 199 cm^{-1} is caused by the shearing vibration of YGe_7. Only one sharp peak in Raman spectra at 209 cm^{-1} results from the breathing vibration of the YGe_7 cluster. The **7A2** isomer belongs to the C_1 point group symmetry. In its IR spectra, the most intense peak at 258 cm^{-1} corresponds to the stretching mode of YGe_7. The second strongest peak at 167 cm^{-1} is caused by the bending vibration of YGe_7. Compared to the **7A1** structure, their peak positions differ by 30 cm^{-1} in IR spectra. In Raman spectra, only one sharp peak at 216 cm^{-1} stems from the breathing vibration of the YGe_7 cluster. It is only different from that of **7A1** by 7 cm^{-1} in Raman spectra.

For n = 8, two configurations are also simulated. **8A1** is part of the C_s point group symmetry. In its IR spectra, there are three dominant peaks. The most intense and largest frequency of 265 cm^{-1} corresponds to the breathing vibration of the Ge_4 tetrahedron formed by the four Ge atoms on the far left of **8A1**. The second and third strongest peaks located at 224 and 180 cm^{-1} stem from the bending mode of YGe_8, respectively. Only one sharp peak in Raman spectra at 219 cm^{-1} stems from the breathing vibration of YGe_8-capped pentagonal bipyramid (except for the outermost Ge atom). **8A2** is part of the C_2 point group symmetry. One sharp peak in IR spectra at 225 cm^{-1} results from the bending mode of the YGe_8 cluster. There are three dominant peaks in its Raman spectra. The most intense peak at 219 cm^{-1} corresponds to the breathing vibration of YGe_8. The second and third strongest peaks located at 277 and 197 cm^{-1} stem from the bending mode of YGe_8, respectively. The YGe_9^- cluster is part of the C_{4v} point group symmetry. The highest frequency at 249 cm^{-1} with IR- and Raman-active characteristics stems from the breathing vibration of YGe_9. The doubly degenerate vibration mode situated at 134 cm^{-1} is a bending mode of YGe_9 and leads to the maximum IR intensity. In Raman spectra, the most intense frequency at 202 cm^{-1} results from the breathing mode of the YGe_9 cluster.

For n = 10, it is part of the C_2 point group symmetry. In its IR and Raman spectra, only one dominant peak of each is observed. The peak at 230 cm^{-1} with IR-active characteristics is the stretching vibration of four Y−Ge bonds and that at 263 cm^{-1} with Raman-active characteristics is the breathing vibration of two Ge_5 (Y atom remains static). For n = 11, it belongs to the C_s point group symmetry. Only one sharp peak in IR spectra at 229 cm^{-1} stems from the stretching mode of

https://doi.org/10.1021/acsomega.2c03983
ACS Omega 2022, 7, 36330−36342

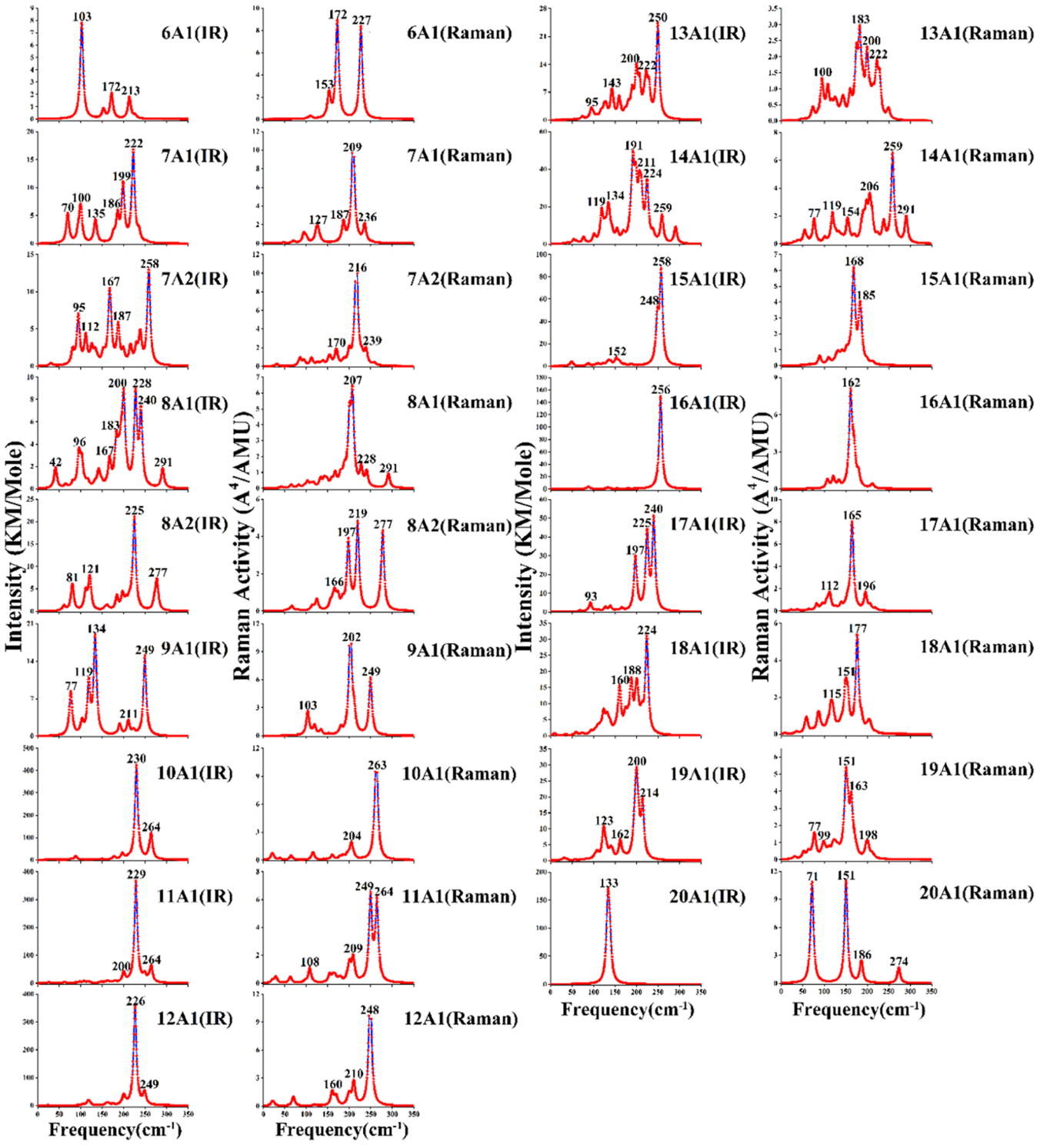

Figure 7. IR and Raman spectra of anionic YGe_n^- (n = 6−20) clusters.

eight Y−Ge bonds. Two most intense peaks in its Raman spectra at 249 and 264 cm^{-1} result from the breathing vibrations of YGe_6 and YGe_5, respectively. For n = 12, it is part of the D_{2d} point group symmetry. It is similar to the YGe_{10}^- cluster. One sharp peak in IR spectra at 226 cm^{-1} stems from the stretching mode of eight Y−Ge bonds, and one dominant peak in Raman spectra at 248 cm^{-1} results from the symmetric breathing mode of two Ge_6 (Y atom remains static). For n = 13, it belongs to the C_s point group symmetry. There are three dominant peaks in its IR and Raman spectra. The most intense peak in IR spectra at 250 cm^{-1} stems from the stretching mode of YGe_{13}. The second and third intense peaks at 200 and 222 cm^{-1} with IR- and Raman-active characteristics result from the bending vibration of YGe_{13}. The strongest peak in Raman spectra at 183 cm^{-1} stems from the breathing vibration of YGe_{13}. For n = 14, it is part of the C_s point group symmetry. The most intense peak of its IR spectra at 191 cm^{-1} stems from the bending mode of YGe_{14}. There are several consecutive shoulder peaks behind the largest peak. In its Raman spectra, the largest peak at 259 cm^{-1} results mainly

https://doi.org/10.1021/acsomega.2c03983
ACS Omega 2022, 7, 36330−36342

from the breathing mode of the Ge_5 subcluster, and the second largest peak at 206 cm^{-1} stems largely from the breathing vibration of Ge_9 TTP.

For n = 15, it is part of the C_{2v} point group symmetry. The most intense peak in IR spectra at 258 cm^{-1} with a shoulder peak at 248 cm^{-1} results from the stretching mode of YGe_{15}. There are two dominant peaks with Raman-active characteristics. They stem from the breathing vibration of Ge_{15} (Y atom remains static). For n = 16, it is part of the T_d point group symmetry. In its IR and Raman spectra, only one sharp peak of each is found. The peak at 256 cm^{-1} with IR-active characteristics is the threefold degenerate stretching modes of YGe_{16} and that at 162 cm^{-1} with Raman-active characteristics stems from the breathing vibration of the Ge_{16} cage (Y atom remains static). For n = 17, it belongs to the C_{4v} point group symmetry. There are three dominant peaks in its IR spectra. The most intense peak at 240 cm^{-1} stems from the stretching mode of YGe_{17}. The remaining two peaks at 225 and 197 cm^{-1} are doubly degenerate modes caused by bending vibrations of YGe_{17}. Only one sharp peak in Raman spectra at 165 cm^{-1} results from the breathing mode of Ge_{17} cage (Y atom remains static). For n = 18, it is part of the C_2 point group symmetry. There are one sharp and three weaker peaks in IR spectra. The sharp peak at 224 cm^{-1} stems from the stretching mode of YGe_{18}. The three peaks at 160−200 cm^{-1} result from the bending vibrations of YGe_{18}. The most intense peak in Raman spectra at 177 cm^{-1} stems from the breathing mode of YGe_{18}. For n = 19, it is part of the C_{2v} point group symmetry. In its IR spectra, the most intense peak at 200 cm^{-1} with a shoulder peak at 214 cm^{-1} stems from the stretching vibrations of YGe_{19}. In its Raman spectra, the strongest peak at 151 cm^{-1} with a shoulder peak at 163 cm^{-1} results from the breathing vibrations of YGe_{19} and Ge_{19} cages (Y atom remains static), respectively. For n = 20, it is part of the I_h point group symmetry. Only one sharp peak at 133 cm^{-1} with IR-active characteristics results from the stretching vibration of the Y atom in the Ge cage. Two dominant peaks in the Raman spectra at 71 and 151 cm^{-1} stem from the bending vibration and breathing mode of the Ge_{20} cage, respectively (Y atom remains static).

From the discussion mentioned above, it can be found that IR and Raman activity testifies different spectra for these clusters and provide information on the effect of structural diversification. The most intense peak in IR spectra is mainly the stretching modes for Y-linked and Y-encapsulated configurations and that in Raman spectra is chiefly the breathing vibrations of the Ge subclusters for the Y-linked motif and Ge cage (Y atom remains static) for the Y-encapsulated structure. The strongest peak in Raman spectra is red-shifted from Y-linked to Y-encapsulated structures. Compared with the far-IR range of nearly 400−10 cm^{-1}, the IR range is shown for these structures. Accordingly, the most stable nanoclusters with the composition could be worthwhile for IR-sensing devices in the far-IR area.

3.5. UV−vis Spectra of the YGe_{16}^- Molecule. In order to further appreciate the optical property of highly thermodynamically and chemically stable YGe_{16}^- nanoclusters, the UV−vis (ultraviolet−visible) spectra were simulated via time-dependent density functional theory (TD-DFT) calculation through the PBE functional with aug-cc-pVDZ and ECP28MWB basis sets for Ge and Y atoms, respectively. To guarantee the computational accuracies, sufficient bands were necessitated to be taken into account, so the 120 excited states were characterized to fulfill the described system. The resulting spectra of the anionic YGe_{16}^- nanocluster are organized by the Gaussian broadening function with 0.25 eV FWHM (full width at half maximum) to distinguish each peak apparently and shown in Figure 8. In the mass, four absorption bands are

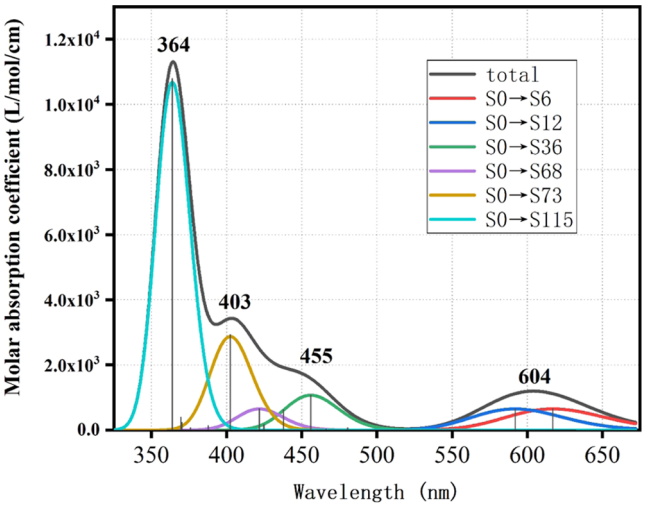

Figure 8. Simulated UV−vis spectra of the anionic YGe_{16}^- superatom.

found in the UV−vis absorption spectrum of the anionic YGe_{16}^- nanocluster; one of them is located in the near-UV section with the other three in the visible section. The first absorption band with the highest peak at 364 nm ranges from 330 to 393 nm. Its highest intensity largely arrives from the $S_0 \rightarrow S_{115}$, accounting for 94%. The second absorption band ranges from 393 to 433 nm. The most intense peak is at 403 nm. It is composed of $S_0 \rightarrow S_{73}$ and $S_0 \rightarrow S_{68}$ with contribution rates of 84 and 8%, respectively. The third absorption band is from 433 to 523 nm. The strongest peak is at 455 nm, which comes primarily from the $S_0 \rightarrow S_{36}$ with a contribution rate of 66%. The fourth absorption band ranges from 523 to 671 nm. The most intense peak is located at 604 nm, which consists of the $S_0 \rightarrow S_{12}$ and $S_0 \rightarrow S_6$ with contribution rates of 51 and 49%, respectively. More importantly, the visible light section (380−671 nm) accounts for 54% of the total region. It can be excited by natural light, particularly with solar energy as energy for driving the photosensitive or optoelectronic device. At the same time, most of the ultraviolet section is at 364 nm, which can be easily excited using UV light-emitting diodes for photoluminescent materials. All in all, the T_d-symmetry anionic YGe_{16}^- FK-cage configuration not only possesses nice optical properties but also possesses perfect chemical and thermodynamic stability, making it the most suitable building block for further development as a potential photosensitive or optoelectronic device.

4. CONCLUSIONS

In short, the ground-state structural evolution behavior of germanium anionic clusters doped with rare-earth metal yttrium, YGe_n^- (n = 6−20), has been investigated using a mPW2PLYP density functional scheme and an ABCluster structure searching technique. It is clearly shown that with the increasing cluster size n, the structure evolution pattern is from the Y-linked framework (n = 10−14) where the Y serves as a linker (the Y atom bridges two germanium subclusters) to the Y-encapsulated framework (n = 15−20) where the Y atom is

https://doi.org/10.1021/acsomega.2c03983
ACS Omega 2022, 7, 36330−36342

located in the center of the germanium cage. The simulated PES spectra show a satisfying agreement with the experimental PES spectra for n = 12−20, which reveals that the GM structures reported here are reliable. In particular, the anionic YGe_{16}^- nanocluster is found to be the most stable structure in the size range of n = 6−20 through analyzes of the relative stability, HOMO−LUMO gap, spherical jellium model, and isochemical shielding surface. Moreover, the spectral properties such as infrared and Raman spectra were reported. These spectra could provide additional ways to experimentally determine the electronic configuration and equilibrium geometry of these clusters. In addition, the UV−vis spectra of the YGe_{16}^- nanocluster is in good agreement with solar energy distribution, showing that such substances serve as multifunctional building blocks to be potentially used in optoelectronic devices or solar energy converters.

■ ASSOCIATED CONTENT

Supporting Information

The Supporting Information is available free of charge at https://pubs.acs.org/doi/10.1021/acsomega.2c03983.

Eigenstate of Ge_{4-6} and Ge_9 subclusters; DOS/PDOS of different anionic YGe_n (n = 6−20) clusters; total energies of YGe_n^- (n = 6−20) clusters; natural population analysis charge and valence electron configuration of Y atom in the global minima YGe_n^- (n = 6−20) compounds; and mPW2PLYP cartesian coordinates of the low-lying isomers of YGe_n^- (n = 6−20) clusters (PDF)

■ AUTHOR INFORMATION

Corresponding Author

Jucai Yang − *School of Chemical Engineering, Inner Mongolia University of Technology, and Inner Mongolia Key Laboratory of Theoretical and Computational Chemistry Simulation, Hohhot 010051, Peoples Republic of China; School of Energy and Power Engineering, Inner Mongolia University of Technology, Hohhot 010051, Peoples Republic of China;* orcid.org/0000-0003-4998-0364; Email: yangjc@imut.edu.cn

Authors

Haibo Wang − *School of Chemical Engineering, Inner Mongolia University of Technology, and Inner Mongolia Key Laboratory of Theoretical and Computational Chemistry Simulation, Hohhot 010051, Peoples Republic of China*

Caixia Dong − *School of Mining and Technology, Inner Mongolia University of Technology, Hohhot 010051, Peoples Republic of China*

Complete contact information is available at: https://pubs.acs.org/10.1021/acsomega.2c03983

Notes

The authors declare no competing financial interest.

■ ACKNOWLEDGMENTS

This work was supported by the National Natural Science Foundation of China (grant no. 21863007), by the Program for Innovative Research Team at University of Inner Mongolia Autonomous Region (grant no. NMGIRT2214), by Inner Mongolia Natural Science Foundation (grant no. 2020LH2003), and by Plan Project in Inner Mongolia Autonomous Region (grant no. JH20180633).

■ REFERENCES

(1) Pillarisetty, R. Academic and Industry Research Progress in Germanium Nanodevices. *Nature* **2011**, *479*, 324−328.

(2) Brattain, W. H.; Bardeen, J. Nature of the Forward Current in Germanium Point Contacts. *Phys. Rev.* **1948**, *74*, No. 231.

(3) Zevallos-Chávez, J.; da Cruz, M. T. F.; Martins, M. N.; Likhachev, V. P.; Zamboni, C. B.; Camargo, S. P.; Genezini, F. A.; Medeiros, J. A. G.; Hindi, M. M. Response Function of a Germanium Detector to Photon Energies between 6 and 120 keV. *Nucl. Instrum. Methods. Phys. Res. A* **2001**, *457*, 212−219.

(4) Moskalyk, R. R. Review of germanium processing worldwide. *Miner. Eng.* **2004**, *17*, 393−402.

(5) Bandyopadhyay, D.; Kaur, P.; Sen, P. New Insights into Applicability of Electron-Counting Rules in Transition Metal Encapsulating Ge Cage Clusters. *J. Phys. Chem. A* **2010**, *114*, 12986−12991.

(6) Yang, Z.; Cao, Z.; Bano, R.; Yang, J.; Gilani, M. A. A Systematic Investigation of Structural Growth Patterns and Electronic Properties of $[LuGe_n]^{+/0}$ and $[Ge_{n+1}]^{+/0}$ (n = 1−17) Nanoalloy Clusters. *Mater. Today Commun.* **2022**, *30*, No. 103018.

(7) Zhao-Feng, Y.; Zhen-Zhu, C.; Rehman, A. U.; Ju-Cai, Y.Structural and Electronic Properties of Lutetium Doped Germanium Clusters $LuGe_n^{(+/0/-)}$ (n = 6-19): A Density Functional Theory Investigation*Chin. J. Struct. Chem.*2022; Vol. *41*2203155−2203165.

(8) Serrano, D.; Kuppusamy, S. K.; Heinrich, B.; Fuhr, O.; Hunger, D.; Ruben, M.; Goldner, P. Ultra-narrow Optical Linewidths in Rare-earth Molecular Crystals. *Nature* **2022**, *603*, 241−246.

(9) Nweke, N.; Runser, R. J.; McNown, S. R.; Khurgin, J. B. Experimental Investigation of Gain Transients in Praseodymium-doped Flfluoride Fifiber Amplifiers. *Opt. Eng.* **2005**, *44*, No. 095004.

(10) Zhang, Y.; Xia, L.; Li, C.; Ding, J.; Li, J.; Zhou, Y. Enhanced 2.7 μm Mid-infrared Emission in Er^{3+}/Ho^{3+} Co-doped Tellurite Glass. *Opt. Laser Technol.* **2021**, *138*, No. 106913.

(11) Tai, T. B.; Nguyen, M. T. A Stochastic Search for the Structures of Small Germanium Clusters and Their Anions: Enhanced Stability by Spherical Aromaticity of the Ge_{10} and Ge_{12}^{2-} Systems. *J. Chem. Theory Comput.* **2011**, *7*, 1119−1130.

(12) Bulusu, S.; Yoo, S.; Zeng, X. C. Search for Global Minimum Geometries for Medium Sized Germanium Clusters: Ge_{12} - Ge_{20}. *J. Chem. Phys.* **2005**, *122*, No. 164305.

(13) An, W. Predicting the Structural Evolution of $Ge_n^-(3\leq n\leq 20)$-Clusters: an Anion Photoelectron Spectroscopy Simulation. *Phys. Chem. Chem. Phys.* **2018**, *20*, 25746−25751.

(14) Borshch, N. A.; Kurganskii, S. I. Atomic Structure and Electronic Properties of Anionic Germanium-Zirconium Clusters. *Inorg. Mater.* **2018**, *54*, 1−7.

(15) Jaiswal, S.; Kumar, V. Growth Behavior and Electronic Structure of Neutral and Anion $ZrGe_n$(n = 1-21) Clusters. *Comput. Theor. Chem.* **2016**, *1075*, 87−97.

(16) Fan, Y. W.; Kong, X. Y.; Zhao, L. J.; Wang, H. Q.; Li, H. F.; Zhan, Q.; Xie, B.; Xu, H. G.; Zheng, W. J. A Joint Experimental and Theoretical Study on Structural, Electronic, and Magnetic Properties of $MnGe_n^-$ (n = 3-14) Clusters. *J. Chem. Phys.* **2021**, *154*, No. 204302.

(17) Trivedi, R.; Mishra, V. Exploring the Structural Stability Order and Electronic Properties of Transition Metal $M@Ge_{12}$(M = Co, Pd, Tc, and Zr) Doped Germanium Cage Clusters-A Density Functional Simulation. *J. Mol. Struct.* **2021**, *1226*, No. 129371.

(18) Boudjahem, A. G.; Boulbazine, M.; Derdare, M. A Theoretical Study of the Stability and Electronic Properties of Ge_nRu(n = 2-10) Clusters and their Sensitivity toward SO_2 Adsorption. *Struct. Chem.* **2020**, *31*, 2341−2353.

(19) Siouani, C.; Mahtout, S.; Rabilloud, F. Structure, Stability, and Electronic Properties of Niobium-Germanium and Tantalum-Germanium Clusters. *J. Mol. Model.* **2019**, *25*, No. 113.

(20) Mahtout, S.; Siouani, C.; Rabilloud, F. Growth Behavior and Electronic Structure of Noble Metal-Doped Germanium Clusters. *J. Phys. Chem. A* **2018**, *122*, 662−677.
(21) Lasmi, M.; Mahtout, S.; Rabilloud, F. Growth Behavior and Electronic and Optical Properties of $IrGe_n$ (n = 1-20) Clusters. *J. Nanopart. Res.* **2021**, *23*, No. 26.
(22) Triedi, R. K.; Bandyopadhyay, D. Insights of the Role of Shell Closing Model and NICS in the Stability of $NbGe_n$ (n = 7-18) Clusters: a First-Principles Investigation. *J. Mater. Sci.* **2019**, *54*, 515−528.
(23) Trivedi, R.; Bandyopadhyay, D. Evolution of Electronic and Vibrational Properties of $M@X_n$ (M = Ag, Au, X = Ge, Si, n = 10, 12, 14) Clusters: a Density Functional Modeling. *J. Mater. Sci.* **2018**, *53*, 8263−8273.
(24) Zhao, J.; Du, Q.; Zhou, S.; Kumar, V. Endohedrally Doped Cage Clusters. *Chem. Rev.* **2020**, *120*, 9021−9163.
(25) Lu, S. J.; Hu, L. R.; Xu, X. L.; Xu, H. G.; Chen, H.; Zheng, W. J. Transition from Exohedral to Endohedral Structures of $AuGe_n^-$ (n = 2-12) Clusters: Photoelectron Spectroscopy and ab Initio Calculations. *Phys. Chem. Chem. Phys.* **2016**, *18*, 20321−20329.
(26) Deng, X. J.; Kong, X. Y.; Xu, X. L.; Xu, H. G.; Zheng, W. J. Photoelectron Spectroscopy and Density Functional Calculations of $TiGe_n^-$(n = 7-12) Clusters. *Chin. J. Chem. Phys.* **2016**, *29*, 123−128.
(27) Deng, X. J.; Kong, X. Y.; Xu, H. G.; Feng, X. G.; Zheng, W. J.; et al. Structural and Magnetic Properties of $FeGe_n^{-/0}$ (n = 3-12) Clusters: Mass-selected Anion Photoelectron Spectroscopy and Density Functional Theory Calculations. *J. Chem. Phys.* **2017**, *147*, No. 234310.
(28) Bandyopadhyay, D. Electronic structure and stability of anionic $AuGe_n$ (*n* = 1-20) clusters and assemblies: a density functional modeling. *Struct. Chem.* **2019**, *30*, 955−963.
(29) Dhaka, K.; Bandyopadhyay, D. Study of the electronic structure, stability and magnetic quenching of $CrGe_n$ (*n* = 1-17) clusters: a density functional investigation. *RSC Adv.* **2015**, *5*, 83004−83012.
(30) Trivedi, R.; Dhaka, K.; Bandyopadhyay, D. Study of electronic properties, stabilities and magnetic quenching of molybdenum-doped germanium clusters: a density functional investigation. *RSC Adv.* **2014**, *4*, 64825−64834.
(31) Kumar, M.; Bhattacharyya, N.; Bandyopadhyay, D. Architecture, electronic structure and stability of $TM@Ge_n$ (TM = Ti, Zr and Hf; *n* = 1-20) clusters: a density functional modeling. *J. Mol. Model.* **2012**, *18*, 405−418.
(32) Bandyopadhyay, D. Architectures, electronic structures, and stabilities of Cu-doped Gen clusters: density functional modeling. *J. Mol. Model.* **2012**, *18*, 3887−3902.
(33) Bandyopadhyay, D.; Kaur, P.; Sen, P. New insights into applicability of electron-counting rules in transition metal encapsulating Ge cage clusters. *J. Phys. Chem. A* **2010**, *114*, 12986−12991.
(34) Bandyopadhyay, D.; Sen, P. Density functional investigation of structure and stability of Ge_n and Ge_nNi (*n* = 1-20) clusters: Validity of the electron counting rule. *J. Phys. Chem. A* **2010**, *114*, 1835−1842.
(35) Jena, P. Superatomic chemistry. *J. Indian Chem. Soc.* **2022**, *99*, No. 100350.
(36) Jena, P.; Sun, Q. Super atomic clusters: design rules and potential for building blocks of materials. *Chem. Rev.* **2018**, *118*, 5755−5870.
(37) Atobe, J.; Koyasu, K.; Furusea, S.; Nakajima, A. Anion Photoelectron Spectroscopy of Germanium and Tin Clusters Containing a Transition- or lanthanide-metal Atom; MGe_n^-(n = 8-20) and MSn_n^- (n = 15-17) (M = Sc-V, Y-Nb, and Lu-Ta). *Phys. Chem. Chem. Phys.* **2012**, *14*, 9403−9410.
(38) Singh, A. K.; Kumar, V.; Kawazoe, Y. Thorium Encapsulated Caged Clusters of Germanium: $Th@Ge_n$, n = 16,18, and 20. *J. Phys. Chem. B* **2005**, *109*, 15187−15189.
(39) Yang, Z. F.; Cao, Z. Z.; Rehman, A. U.; Yang, J. C. Structural Evolution, Electronic Structures, and Vibrational Properties of Anionic $LuGe_n$ (n = 5-17) Clusters: From Lu-Linked to Lu-Encapsulated Configurations. *Inorg. Chem.* **2021**, *60*, 14446−14456.
(40) Yang, Z. F.; Rehman, A. U.; Cao, Z. Z.; Yang, J. C. Structural evolution, photoelectron spectra and vibrational properties of anionic $GdGe_n^-$ (*n* = 5-18) nanoalloy clusters: a DFT insight. *RSC Adv.* **2022**, *12*, 22020−22030.
(41) Zhang, J.; Dolg, M. ABCluster: the Artificial Bee Colony Algorithm for Cluster Global Optimization. *Phys. Chem. Chem. Phys.* **2015**, *17*, 24173−24181.
(42) Zhang, J.; Dlog, M. Global Optimization of Clusters of Rigid Moleculesby the Artifificial Bee Colony Algorithm. *Phys. Chem. Chem. Phys.* **2016**, *18*, 3003−3010.
(43) Zhang, J.; Glezakou, V. A.; Rousseau, R.; Nguyen, M. TNWPEsSe: An Adaptive-Learning Global Optimization Algorithm for Nanosized Cluster Systems. *J. Chem. Theory Comput.* **2020**, *16*, 3947−3958.
(44) Frisch, M. J.; Trucks, G. W.; Schlegel, H. B.; Scuseria, G. E.; Robb, M. A.; Cheeseman, J. R.; Scalmani, G.; Barone, V.; Mennucci, B.; Petersson, G. A.; Nakatsuji, H.et al.*Gaussian 09*, Revision C.01; Gaussian, Inc.: Wallingford CT, 2010.
(45) Adamo, C.; Barone, V. Toward Reliable Density Functional Methods without Adjustable Parameters: The PBE0 Model. *J. Chem. Phys.* **1999**, *110*, 6158−6169.
(46) Peterson, K. A. Systematically Convergent Basis Sets with Relativistic Pseudopotentials. I. Correlation Consistent Basis Sets for the Post-d Group 13-15 Elements. *J. Chem. Phys.* **2003**, *119*, 11099−11112.
(47) Hay, P. J.; Wadt, W. R. Ab Initio Effective Core Potentials for Molecular Calculations. Potentials for K to Au Including the Outermost Core Orbitals. *J. Chem. Phys.* **1985**, *82*, 299−310.
(48) Andrae, D.; HauBermann, U.; Dolg, M.; Stoll, H.; PreuB, H. Energy-Adjusted Ab Initio Pseudopotentials for the Second and Third Row Transition Elements. *Theor. Chim. Acta.* **1990**, *77*, 123−141.
(49) Martin, J. M. L.; Sundermann, A. Correlation Consistent Valence Basis Sets for Use with the Stuttgart-Dresden-Bonn Relativistic Effective Core Potentials: The Atoms Ga-Kr and In-Xe. *J. Chem. Phys.* **2001**, *114*, 3408−3420.
(50) Jaiswal, S.; Babar, V. P.; Kumar, V. Growth Behavior, Electronic Structure, and Vibrational Properties of Si_nY Anion Clusters (n = 4-20): Metal Atom as Linker and Endohedral Dopant. *Phys. Rev. B* **2013**, *88*, No. 085412.
(51) Schwabe, T.; Grimme, S. Towards Chemical Accuracy for the Thermodynamics of Large Molecules: New Hybrid Density Functionals Including Non-Local Correlation Effects. *Phys. Chem. Chem. Phys.* **2006**, *8*, 4398−4401.
(52) Wilson, A. K.; Woon, D. E.; Peterson, K. A.; Dunning, T. H., Jr. Gaussian Basis Sets for Use in Correlated Molecular Calculations. IX. The Atoms Gallium Through Krypton. *J. Chem. Phys.* **1999**, *110*, 7667−7676.
(53) Lu, T.; Chen, F. Multiwfn: A Multifunctional Wavefunction Analyzer. *J. Comput. Chem.* **2012**, *33*, 580−592.
(54) Ortiz, J. V. Electron Binding Energies of Anionic Alkali Mmetal Atoms from Partial Fourth Order Electron Propagator Theory Calculations. *J. Chem. Phys.* **1988**, *89*, 6348−6352.
(55) Liu, Y.; Yang, J.; Cheng, L. Structural Stability and Evolution of Scandium-Doped Silicon Clusters: Evolution of Linked to Encapsulated Structures and Its Influence on the Prediction of Electron Affinities for $ScSi_n$ (n = 4-16) Clusters. *Inorg. Chem.* **2018**, *57*, 12934−12940.
(56) Liu, B.; Yang, J. Thermochemical Properties and Growth Mechanism of the AgDoped Germanium Clusters, $AgGe_n^{\lambda}$ with n = 1-13 and λ = −1, 0, and +1. *ACS Omega* **2021**, *6*, 9813−9827.
(57) Liu, B.; Wang, X.; Yang, J. Comparative Research of Configuration, Stability and Electronic Properties of Cationic and Neutral $[AuGe_n]^{\lambda}$ and $[Ge_{n+1}]^{\lambda}$(n = 1-13,λ = 0, +1) nanoalloy clusters. *Mater. Today Commun.* **2021**, *26*, No. 101989.
(58) Hostutler, D. A.; Li, H. Y.; Clouthier, D. J.; Wannous, G. Exploring the Bermuda Triangle of Homonuclear Diatomic Spectroscopy: The Electronic Spectrum and Structure of Ge_2. *J. Chem. Phys.* **2002**, *116*, 4135−4141.

https://doi.org/10.1021/acsomega.2c03983
ACS Omega 2022, 7, 36330−36342

(59) Neckel, A.; Sodeck, G. Bestimmung der Dissoziationsenergien der gasformigen Molekule CuGe, AgGe und AuGe. *Monatsh. Chem.* **1972**, *103*, 367−382.
(60) Kingcade, J. E., Jr.; Choudary, U. V.; Gingerich, K. A. Stability and Thermodynamics of Ligand-Free Germanium-Gold Clusters. *Inorg. Chem.* **1979**, *18*, 3095−3104.
(61) Arnold, C. C.; Xu, C.; Burton, G. R.; Neumark, D. M. Study of the Low-Lying States of Ge_2 and Ge_2^- Using Negative Ion Zero Electron Kinetic Energy Spectroscopy. *J. Chem. Phys.* **1995**, *102*, 6982−6989.
(62) Liu, Y.; Yang, J.; Li, S.; Cheng, L. Structural Growth Pattern of Neutral and Negatively Charged Yttrium-Doped Silicon Clusters $YSi_n^{0/-}$ (n = 6-20): from Linked to Encapsulated Structures. *RSC Adv.* **2019**, *9*, 2731−2739.
(63) Baerends, E. J.; Gritsenko, O. V.; Van Meer, R. The Kohn-Sham Gap, the Fundamental Ggap and the Optical Gap: the Physical Meaning of Occupied and Virtual Kohn-Sham Orbital Energies. *Phys. Chem. Chem. Phys.* **2013**, *15*, 16408−16425.
(64) Furuse, S.; Koyasu, K.; Atobe, J.; Nakajima, A. Experimental and Theoretical Characterization of MSi_{16}^-, MGe_{16}^-,MSn_{16}^-, and MPb_{16}^-(M = Ti, Zr, and Hf): The Role of Cage Aromaticity. *J. Chem. Phys.* **2008**, *129*, No. 064311.
(65) Klod, S.; Kleinpeter, E. Ab initio calculation of the anisotropy effect of multiple bonds and the ring current effect of arenes − application in conformational and configurational analysis. *J. Chem. Soc. Perkin Trans. 2* **2001**, 1893−1898.
(66) Zubarev, D. Y.; Boldyrev, A. I. Developing paradigms of chemical bonding: adaptive natural density partitioning. *Phys. Chem. Chem. Phys.* **2008**, *10*, 5207−5217.

https://doi.org/10.1021/acsomega.2c03983
ACS Omega 2022, 7, 36330−36342